

3D Numerical Investigation of Savonius Vertical Axis Wind Turbine using Fluid-Driven 6DoF Motion Solver

Prakash Poudel¹, Pranay Pandey², Manabendra M. De³, and Chandan Bose⁴

¹ Aerospace Engineering, IOE Pulchowk Campus, Tribhuvan University, NEPAL

² FOSSEE, Indian Institute of Technology, Bombay, India

³ Assistant Professor, Academy of Scientific and Innovative Research (AcSIR), New Delhi, INDIA

⁴ Assistant Professor, Aerospace Engineering

College of Engineering and Physical Sciences, University of Birmingham, UK

Abstract

This study presents a 3D numerical investigation of a Savonius vertical axis wind turbine (VAWT) rotor using a fluid-driven approach with OpenFOAM's 6 Degree of Freedom (6DoF) rigid body motion solver. Unlike traditional prescribed motion methods, this work employs the `sixDoFRigidBodyMotion` solver coupled with transient AMI sliding mesh techniques and a spherical angular damper to simulate realistic turbine dynamics under aerodynamic loading. The rotor motion is constrained to rotate about a vertical axis through point and axis constraints, while a calibrated damping coefficient achieves equilibrium at a tip speed ratio (TSR) of 0.585. A comprehensive mesh independence study validates the computational setup across three mesh resolutions. Performance characteristics including power coefficient (C_p), torque coefficient (C_q), and thrust coefficient (C_T) are analyzed at the equilibrium TSR value.

Keywords: Vertical Axis Wind Turbine, Savonius Rotor, 6DoF Rigid Body Motion, Spherical Angular Damper, Computational Fluid Dynamics, OpenFOAM, Mesh Independence Study

1 Introduction

Vertical Axis Wind Turbines (VAWTs) offer distinct advantages for urban and distributed energy applications due to their omnidirectional operation, simple mechanical design, and tolerance to turbulent flow conditions. Among VAWT configurations, the Savonius rotor—a drag-based design—exhibits superior low-speed startup characteristics and requires minimal maintenance, making it particularly suitable for small-scale renewable energy systems [1, 2].

Despite these advantages, conventional Savonius rotors suffer from relatively low power coefficients and negative torque regions that impede performance optimization. Extensive research has focused on geometric modifications including overlap ratios [2], blade profiles [3], helical configurations [4], and multi-stage designs [5]. Recent investigations have explored twisted blade geometries [6] and bio-inspired shapes [7], demonstrating performance improvements of 14-75% over baseline designs.

Numerical investigations of VAWT performance traditionally employ either Multiple Reference Frame (MRF) methods for steady-state approximations or prescribed motion approaches using sliding mesh techniques. While MRF offers computational efficiency, it fails to capture dynamic flow-structure interactions critical for accurate torque prediction in drag-type turbines. Prescribed motion methods, utilizing Arbitrary Mesh Interface (AMI) or similar sliding mesh approaches, provide improved accuracy but impose externally defined rotational velocities that do not reflect realistic turbine response to aerodynamic loading [8].

This study addresses these limitations by implementing a fluid-driven simulation framework using OpenFOAM's 6 Degree of Freedom (6DoF) rigid body motion solver coupled with transient AMI sliding mesh techniques. This approach allows the turbine to respond naturally to fluid forces while incorporating generator loading effects through spherical angular damper. The rotor dynamics are governed by the full rigid body equations of motion, constrained to single-axis rotation through point and axis constraints, representing a more physically realistic model than prescribed motion methods.

The primary objectives of this investigation are:

1. Develop and validate a fluid-driven simulation framework for Savonius VAWT rotors using 6DoF rigid body motion solver
2. Conduct a comprehensive mesh independence study to establish grid convergence
3. Characterize rotor performance across varying tip speed ratios through analysis of power, torque, and thrust coefficients
4. Compare fluid-driven simulation results with traditional prescribed motion approaches to quantify methodological differences

5. Provide insights into dynamic torque variations and flow physics around the Savonius rotor

This work extends the computational methodology established by [8] for bio-inspired rotors to conventional Savonius configurations, while introducing a physically consistent fluid-structure interaction framework applicable to small-scale wind energy systems.

2 Problem Statement

The accurate prediction of Savonius rotor performance under realistic operating conditions requires computational methodologies that simultaneously capture unsteady flow physics and the dynamic response of the turbine structure to aerodynamic loading. Traditional numerical approaches for vertical axis wind turbines face critical limitations in representing this coupled fluid-structure interaction (FSI) and generator loading:

1. **Prescribed Motion Limitations (Kinematic Decoupling):** Conventional transient simulations utilize sliding mesh techniques by imposing an externally defined, constant rotational velocity. This approach forces the kinematics as an input boundary condition rather than letting it emerge naturally from fluid forces, making it fundamentally incapable of predicting self-starting capabilities or dynamic behavior during wind transients.
2. **Omission of Generator Loading:** Real wind turbines operate against an electromagnetic generator resistance that continuously extracts mechanical power and dictates the turbine's operational speed. Traditional CFD methods either completely neglect this resistive torque or approximate it post-simulation using simplified, offline mathematical corrections, leading to artificial operating points.
3. **Steady-State Approximations (MRF Deficiencies):** Simplified approaches, such as the Multiple Reference Frame (MRF) method, treat the rotating domain using a pseudo-steady formulation. For drag-driven turbines like the Savonius rotor where geometry and flow separation change continuously with the azimuthal angle, steady-state models fail to capture vital transient phenomena like blade-wake interactions and structural torque ripples.

To overcome these limitations and achieve a highly realistic representation of turbine operation, this study transitions from an artificial kinematic framework to a true fluid-driven Fluid-Structure Interaction (FSI) methodology. By coupling OpenFOAM's 6 Degree of Freedom (6DoF) rigid body motion solver with transient AMI sliding mesh techniques, the rotor's angular velocity is converted from a static input parameter into an active solution output governed by Newton's second law of rotation.

The traditional challenge of representing generator resistance is directly resolved by implementing a spherical angular damper restraint. This restraint applies a physics-based braking torque that is strictly proportional to the rotor's instantaneous angular velocity, perfectly mimicking the electromagnetic torque extraction of a real generator under electrical load. Consequently, the turbine can autonomously start from rest, accelerate through transient flow regimes, and settle into a stable, continuous equilibrium speed where aerodynamic torque matches generator load. This allows the true operational Tip Speed Ratio (TSR) and performance metrics to emerge naturally from the physics of the simulation.

The successful implementation of this fluid-driven framework enables:

- Direct physics-based prediction of self-starting behavior, transient startup acceleration, and time-to-threshold operational velocity.
- Comprehensive evaluation of load-dependent performance curves by systematically calibrating the damper coefficient rather than prescribing artificial speeds.
- High-fidelity tracking of instantaneous aerodynamic torque variations critical for downstream structural and generator shaft fatigue analysis.
- Validation of traditional, simplified prescribed-motion paradigms through direct comparison with fully coupled fluid-driven data.

3 Governing Equations and Models

This section provides a comprehensive overview of the mathematical framework governing the coupled fluid-structure interaction problem. The simulation solves the incompressible Navier-Stokes equations for the fluid domain while simultaneously integrating the rigid body equations of motion for the rotor, with conservative interpolation across sliding mesh interfaces.

3.1 Fluid Dynamics Equations

The flow field around the Savonius rotor is governed by the incompressible Navier-Stokes equations under the assumption of laminar flow at Reynolds number $Re = \rho U_\infty D / \mu$.

3.1.1 Continuity Equation

Mass conservation requires:

$$\nabla \cdot \mathbf{u} = 0 \tag{1}$$

where \mathbf{u} is the velocity vector field.

3.1.2 Momentum Equation

The conservation of momentum is expressed as:

$$\frac{\partial \mathbf{u}}{\partial t} + \nabla \cdot (\mathbf{u}\mathbf{u}) = -\nabla p + \nu \nabla^2 \mathbf{u} \quad (2)$$

where:

- p is the kinematic pressure (pressure divided by density)
- ν is the kinematic viscosity
- t is time

These equations are solved in the entire computational domain using the finite volume method with the PIMPLE (merged PISO-SIMPLE) algorithm for pressure-velocity coupling in transient simulations.

3.2 Arbitrary Mesh Interface (AMI) Interpolation

The computational domain is partitioned into stationary and rotating regions separated by non-conformal cyclic interfaces. The Arbitrary Mesh Interface technique enables conservative transfer of flow variables across these sliding mesh boundaries.

3.2.1 Conservative Flux Interpolation

At each AMI interface pair, fluxes are interpolated to ensure conservation of mass and momentum. For a conserved variable ϕ , the flux through the interface is transferred from source faces to target faces through weighted interpolation:

$$\Phi_{\text{target}} = \sum_{i \in \text{source}} w_i \phi_i A_i \cdot \mathbf{n}_i \rightarrow \sum_{j \in \text{target}} \phi_j A_j \cdot \mathbf{n}_j \quad (3)$$

where:

- ϕ_i and ϕ_j are the field values on source and target faces
- A_i and A_j are the face areas
- \mathbf{n}_i and \mathbf{n}_j are the face normal vectors
- w_i are interpolation weights

3.2.2 Area-Weighted Averaging

The interpolation scheme employs area-weighted averaging to maintain flux conservation. For each target face, contributions from overlapping source faces are weighted by their projected intersection areas:

$$w_i = \frac{A_{\text{overlap},i}}{\sum_k A_{\text{overlap},k}} \quad (4)$$

This conservative interpolation ensures global mass conservation across the AMI interface despite mesh non-conformity, which is critical for accurate force prediction on the rotor surface.

3.3 Six Degree of Freedom Rigid Body Motion

The rotor dynamics are governed by Newton's laws for rigid body motion, integrated simultaneously with the fluid equations to capture fluid-structure interaction.

3.3.1 Translational Motion

The equation governing the center of mass translation is:

$$m \frac{d\mathbf{v}_c}{dt} = \mathbf{F}_{\text{aero}} + \mathbf{F}_{\text{gravity}} + \mathbf{F}_{\text{constraint}} \quad (5)$$

where:

- m is the rotor mass
- \mathbf{v}_c is the velocity of the center of mass
- \mathbf{F}_{aero} is the total aerodynamic force computed by integrating pressure and viscous stresses over the rotor surface
- $\mathbf{F}_{\text{gravity}} = m\mathbf{g}$ is the gravitational force
- $\mathbf{F}_{\text{constraint}}$ represents constraint forces from kinematic restrictions

3.3.2 Rotational Motion

The angular momentum equation in the body-fixed reference frame is:

$$\mathbf{I} \cdot \frac{d\boldsymbol{\omega}}{dt} + \boldsymbol{\omega} \times (\mathbf{I} \cdot \boldsymbol{\omega}) = \boldsymbol{\tau}_{\text{aero}} + \boldsymbol{\tau}_{\text{damper}} + \boldsymbol{\tau}_{\text{constraint}} \quad (6)$$

where:

- \mathbf{I} is the moment of inertia tensor about the center of mass
- $\boldsymbol{\omega}$ is the angular velocity vector
- $\boldsymbol{\tau}_{\text{aero}}$ is the aerodynamic torque computed from surface pressure and shear stress distributions
- $\boldsymbol{\tau}_{\text{damper}}$ represents generator loading (detailed in Section 3.6)
- $\boldsymbol{\tau}_{\text{constraint}}$ are constraint torques from kinematic restrictions
- The term $\boldsymbol{\omega} \times (\mathbf{I} \cdot \boldsymbol{\omega})$ accounts for gyroscopic effects

3.3.3 Aerodynamic Force and Torque Calculation

The aerodynamic forces and moments are computed by integrating pressure and viscous stresses over the rotor surface S :

$$\mathbf{F}_{\text{aero}} = \int_S (-p\mathbf{n} + \boldsymbol{\tau}_{\text{visc}} \cdot \mathbf{n}) dS \quad (7)$$

$$\boldsymbol{\tau}_{\text{aero}} = \int_S \mathbf{r} \times (-p\mathbf{n} + \boldsymbol{\tau}_{\text{visc}} \cdot \mathbf{n}) dS \quad (8)$$

where:

- \mathbf{n} is the outward surface normal
- $\boldsymbol{\tau}_{\text{visc}} = \mu(\nabla\mathbf{u} + \nabla\mathbf{u}^T)$ is the viscous stress tensor
- \mathbf{r} is the position vector from the center of rotation to the surface element

3.4 Moment of Inertia Tensor

The moment of inertia tensor \mathbf{I} is defined in the principal axes reference frame as:

$$\mathbf{I} = \begin{bmatrix} I_{xx} & 0 & 0 \\ 0 & I_{yy} & 0 \\ 0 & 0 & I_{zz} \end{bmatrix} \quad (9)$$

where I_{xx} , I_{yy} , and I_{zz} are the principal moments of inertia calculated from the CAD geometry mass distribution. The center of mass is located at position $\mathbf{r}_c = (x_c, y_c, z_c)$ in the global coordinate system.

3.5 Kinematic Constraints

To restrict the 6DoF motion to single-axis rotation representative of bearing-mounted VAWT configurations, two constraints are imposed:

3.5.1 Point Constraint

The center of rotation is fixed at the hinge point:

$$\mathbf{r}_{\text{hinge}} = (x_h, y_h, z_h) \quad (10)$$

This constraint eliminates all three translational degrees of freedom, setting $\mathbf{v}_c = \mathbf{0}$.

3.5.2 Axis Constraint

Rotation is restricted to occur about a specified axis direction:

$$\mathbf{a}_{\text{hinge}} = (a_x, a_y, a_z) \quad (11)$$

with $|\mathbf{a}_{\text{hinge}}| = 1$. This constraint eliminates two rotational degrees of freedom, restricting the angular velocity to:

$$\boldsymbol{\omega} = \omega \mathbf{a}_{\text{hinge}} \quad (12)$$

where ω is the scalar angular velocity magnitude.

3.6 Spherical Angular Damper

Generator loading is modeled through a spherical angular damper that applies a resistive torque opposing rotation. The damping torque is proportional to the angular velocity:

$$\boldsymbol{\tau}_{\text{damper}} = -c_{\text{damp}} \boldsymbol{\omega} \quad (13)$$

where c_{damp} is the damping coefficient with units of $\text{N}\cdot\text{m}\cdot\text{s}/\text{rad}$, representing the electromagnetic resistance of the electrical generator.

3.6.1 Equilibrium Condition

At steady-state operation, the aerodynamic torque balances the damping torque:

$$\tau_{\text{aero}} = c_{\text{damp}} \omega_{\text{eq}} \quad (14)$$

where ω_{eq} is the equilibrium angular velocity. This balance determines the operational tip speed ratio:

$$TSR_{eq} = \frac{\omega_{eq} R}{U_{\infty}} \quad (15)$$

where R is the rotor radius and U_{∞} is the freestream velocity.

3.7 Performance Coefficients

The aerodynamic performance of the rotor is characterized using dimensionless coefficients defined as follows:

3.7.1 Power Coefficient

The power coefficient quantifies the efficiency of kinetic energy extraction from the wind:

$$C_p = \frac{P}{\frac{1}{2} \rho A U_{\infty}^3} = \frac{\tau \cdot \omega}{\frac{1}{2} \rho A U_{\infty}^3} \quad (16)$$

where:

- $P = \tau \cdot \omega$ is the mechanical power output
- ρ is the air density
- $A = H \times D$ is the rotor frontal area (height \times diameter)
- U_{∞} is the freestream velocity

3.7.2 Torque Coefficient

The torque coefficient non-dimensionalizes the aerodynamic moment:

$$C_q = \frac{\tau}{\frac{1}{2} \rho A U_{\infty}^2 R} \quad (17)$$

where τ is the instantaneous or cycle-averaged torque.

3.7.3 Thrust Coefficient

The thrust coefficient characterizes the drag force acting on the rotor in the streamwise direction:

$$C_T = \frac{F_x}{\frac{1}{2} \rho A U_{\infty}^2} \quad (18)$$

where F_x is the thrust force component parallel to the incoming flow.

3.7.4 Tip Speed Ratio

The tip speed ratio is the dimensionless parameter relating rotor rotational speed to wind speed:

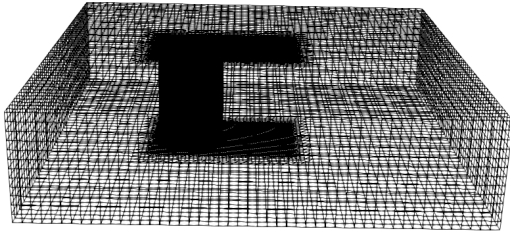
$$\text{TSR} = \lambda = \frac{\omega R}{U_\infty} \quad (19)$$

4 Simulation Procedure

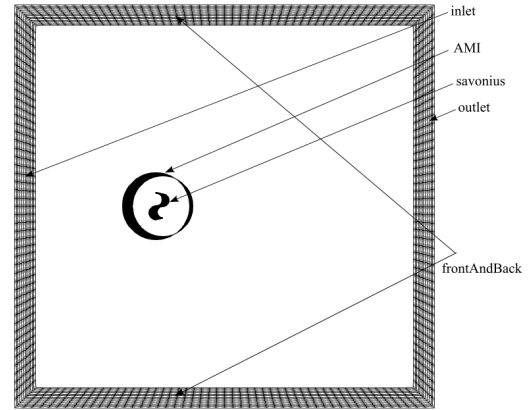
4.1 Geometry and Mesh

4.1.1 Computational Domain

The computational domain is configured to minimize blockage effects while maintaining computational efficiency. The domain extends 400 mm upstream of the rotor centerline, 850 mm downstream, and ± 560 mm in the lateral (Z) direction, with a height of 300 mm corresponding to the rotor height. Figure 1 illustrates the computational domain configuration.



(a) Domain's 3D view



(b) Domain's Top-Down view

Figure 1: Computational domain showing inlet, outlet, and boundary extents

The domain dimensions relative to rotor diameter D are approximately $5D$ upstream, $10D$ downstream, and $14D$ in the spanwise direction, ensuring fully developed flow conditions and negligible wall interference effects. A cylindrical rotating region with diameter $2D$ and height equal to the domain height is defined concentrically around the rotor to facilitate the 6DoF motion and AMI interface implementation.



Figure 2: Savonius rotor CAD geometry with characteristic dimensions $H = 300\text{mm}$, $D = 82\text{mm}$

The Savonius rotor geometry (Figure 2) features two semi-circular blades arranged in the conventional configuration with height-to-diameter ratio $H/D = 3.66$. The rotor is positioned such that its center of rotation coincides with the origin of the rotating cylindrical zone.

4.1.2 Mesh Generation Strategy

The computational mesh is generated using OpenFOAM's native utilities following a hierarchical refinement strategy. The mesh generation workflow consists of three stages. First, `blockMesh` creates a structured hexahedral background mesh spanning the entire computational domain based on the vertex coordinates defined in `blockMeshDict`. This base mesh provides uniform cell distribution with appropriate overall resolution. Second, `snappyHexMesh` performs castellated mesh refinement and geometry conforming operations. The castellated meshing stage refines cells intersecting predefined refinement regions particularly the rotating zone and wake region through recursive hex-cell splitting. The rotor surface geometry, imported as a 3D object file (.obj format), is then captured through surface snapping where mesh vertices are projected onto the geometry surface to accurately represent the curved blade profiles. Finally, `topoSet` defines the cylindrical `rotatingZone` cell set and creates the AMI interface patches separating the stationary and rotating regions.

4.1.3 Mesh Independence Study

A systematic mesh independence study was conducted to establish grid convergence and select an appropriate mesh resolution for production simulations. Three progressively refined meshes were

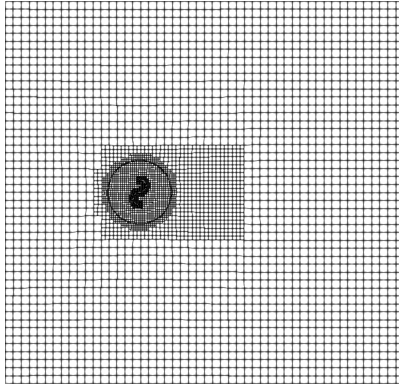
generated by varying the refinement levels. Simulations were performed at equilibrium tip speed ratio (TSR) with the power coefficient (C_p) serving as the primary convergence metric.

Table 1 summarizes the mesh characteristics and predicted performance coefficients.

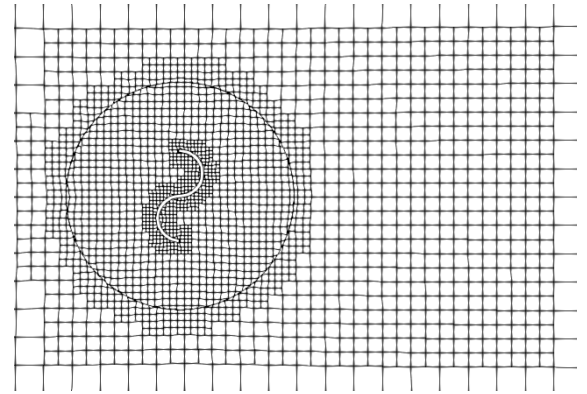
Table 1: Mesh independence study results at equilibrium TSR = 0.585

Mesh	Total Cells	Rotor Zone Cells	C_p	Relative Error (%)
Coarse	125880	66427	0.1799	—
Medium	378824	249912	0.1813	0.772%
Fine	528884	305472	0.1816	0.165%

Figures 3, 4, 5 and 6 present the mesh configurations and convergence behavior.

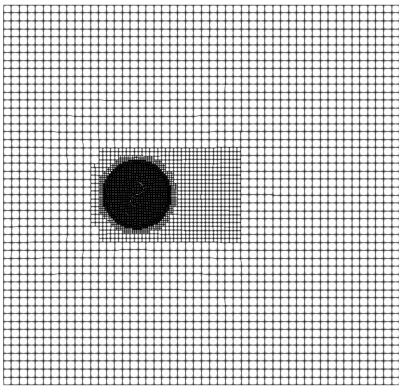


(a) Coarse mesh Top-Down view

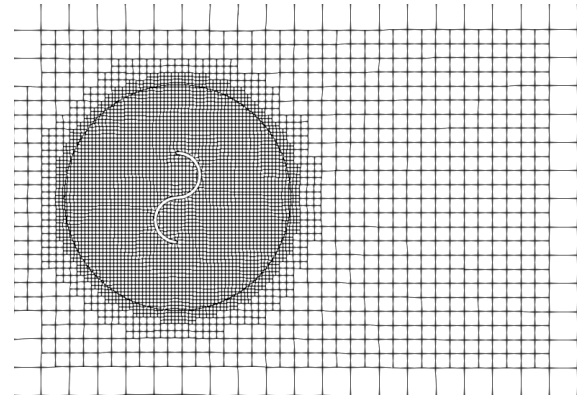


(b) Coarse mesh close view

Figure 3: Coarse Mesh configurations for independence study

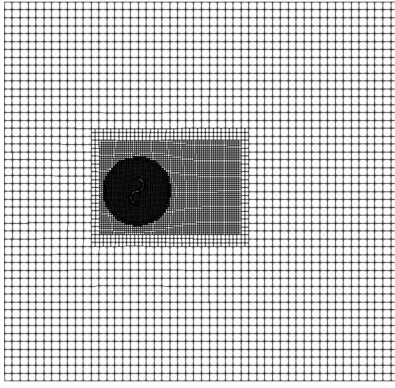


(a) Medium mesh Top-Down view

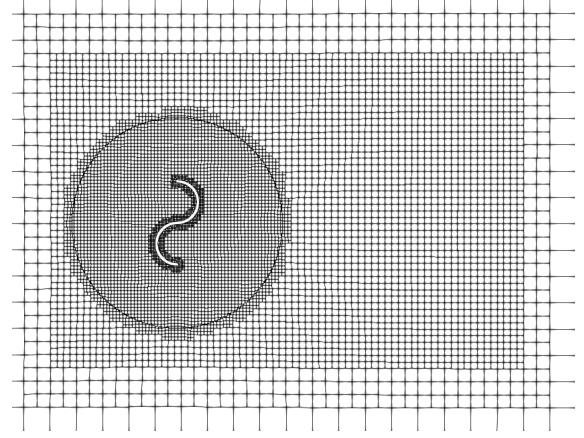


(b) Medium mesh close view

Figure 4: Medium Mesh configurations for independence study



(a) Fine mesh Top-Down view



(b) Fine mesh close view

Figure 5: Fine Mesh configurations for independence study

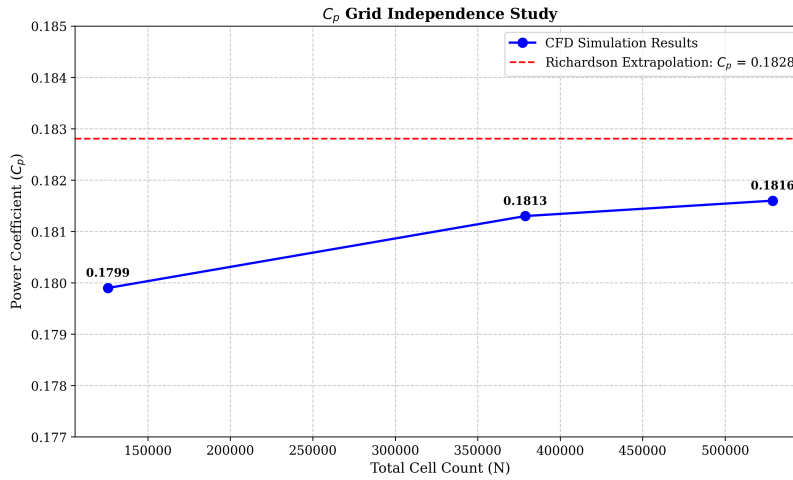


Figure 6: Power coefficient variation with total cell count

The convergence plot (Figure 6) demonstrates an asymptotic approach to a grid-independent solution with increasing mesh refinement. Although Richardson extrapolation suggests that further refinement to $C_p = 0.1836$ would improve accuracy, such refinement was not pursued due to severe computational constraints inherent to the coupled 6DoF-AMI approach. Each additional mesh refinement level increases computational time by a factor of 3-4, making a 5 million+ cell mesh impractical within project timescales and computational resources. Therefore the finer mesh was selected as it converges towards the interpolated data and has low relative error.

4.2 Initial and Boundary Conditions

The boundary conditions are specified to simulate uniform approach flow with atmospheric properties under laminar flow assumptions. Table 2 summarizes the conditions applied to each patch in the computational domain.

Table 2: Boundary conditions for pressure and velocity fields

Patch	Pressure p	Velocity \mathbf{u}
inlet	zeroGradient	fixedValue ($U_\infty, 0, 0$)
outlet	fixedValue 0	zeroGradient
lowerWall	zeroGradient	zeroGradient
upperWall	zeroGradient	zeroGradient
frontAndBack	zeroGradient	zeroGradient
savonius	fixedFluxPressure	movingWallVelocity
AMI1	cyclicAMI	cyclicAMI
AMI2	cyclicAMI	cyclicAMI

The `fixedFluxPressure` boundary condition on the rotor surface adjusts the pressure gradient to be consistent with the velocity boundary condition, which is critical for moving wall boundaries. The `movingWallVelocity` condition automatically computes the surface velocity based on the 6DoF solver motion, ensuring no-slip conditions in the rotating reference frame. The `cyclicAMI` patches handle the non-conformal interface between stationary and rotating regions with conservative flux interpolation.

4.2.1 Initial Conditions

The simulation is initialized from rest with the following initial state:

- Pressure field: $p = 0$ Pa (gauge pressure)
- Velocity field: $\mathbf{u} = (U_\infty, 0, 0)$ m/s throughout the domain
- Rotor angular velocity: $\omega_0 = 0$ rad/s
- Rotor linear velocity: $\mathbf{v}_c = (0, 0, 0)$ m/s
- Rotor position: centered at origin with initial azimuthal orientation $\theta_0 = 0^\circ$

4.2.2 Fluid Properties

Standard atmospheric air properties are employed:

- Density: $\rho = 1.225 \text{ kg/m}^3$
- Dynamic viscosity: $\mu = 1.8375 \times 10^{-5} \text{ kg/(m}\cdot\text{s)}$
- Kinematic viscosity: $\nu = \mu/\rho = 1.5 \times 10^{-5} \text{ m}^2/\text{s}$

For an inlet velocity of $U_\infty = 5 \text{ m/s}$ and rotor diameter $D = 82 \text{ mm}$, the Reynolds number is:

$$Re = \frac{U_\infty D}{\nu} = \frac{5 \times 0.082}{1.5 \times 10^{-5}} \approx 28,000$$

This moderately low Reynolds number justifies the laminar flow assumption employed in the simulations.

4.2.3 6DoF Motion Parameters

The rigid body motion solver requires specification of the rotor's inertial properties:

- Mass: $m = 0.1405 \text{ kg}$
- Center of mass: $\mathbf{r}_c = (21.25, 150, 41) \text{ mm}$
- Moment of inertia tensor (principal axes):

$$\mathbf{I} = \begin{bmatrix} 1.138 \times 10^{-3} & 0 & 0 \\ 0 & 1.117 \times 10^{-4} & 0 \\ 0 & 0 & 1.080 \times 10^{-3} \end{bmatrix} \text{ kg}\cdot\text{m}^2$$

- Hinge point (center of rotation): $\mathbf{r}_h = (21.25, 150, 41) \text{ mm}$
- Rotation axis: $\mathbf{a}_h = (0, 1, 0)$
- Damping coefficient: $c_{\text{damp}} = 6.28 \times 10^{-5} \text{ N}\cdot\text{m}\cdot\text{s/rad}$

The moment of inertia values were calculated from the CAD model using the material density and geometric distribution. The hinge point coincides with the center of mass to eliminate coupling between translational and rotational dynamics.

4.3 Solver Configuration

4.3.1 Solver Setup

The simulations utilize `pimpleFoam`, OpenFOAM's incompressible transient solver designed for moving mesh applications. This solver implements the PIMPLE algorithm which is a hybrid approach merging PISO (Pressure Implicit with Splitting of Operators) and SIMPLE (Semi-Implicit Method for Pressure-Linked Equations) to achieve robust pressure-velocity coupling in transient scenarios.

The algorithm iterates between momentum prediction, pressure correction, and velocity correction until convergence criteria are satisfied at each time step. Outer corrector loops ensure proper coupling between the flow solution and mesh motion.

4.3.2 Dynamic Mesh Configuration

The dynamic mesh functionality is configured through the `dynamicMeshDict` file with the following key specifications:

- Dynamic mesh type: `dynamicMotionSolverFvMesh`
- Motion solver library: `sixDoFRigidBodyMotion`
- Motion solver: `sixDoFRigidBodyMotion`

The AMI patches are configured as `cyclicAMI` boundary types, enabling periodic coupling with automatic overlap calculation and flux interpolation as the rotating region moves.

4.3.3 Discretization Schemes

Table 3 details the numerical discretization schemes employed for spatial and temporal derivatives.

Table 3: Discretization schemes (fvSchemes)

Term	Parameter	Scheme
Time derivative	<code>ddtSchemes default</code>	Euler
Gradient	<code>gradSchemes default</code>	Gauss linear
Divergence	<code>div(phi,U)</code> <code>div((nuEff*dev2(T(grad(U)))))</code>	Gauss linearUpwind grad(U) Gauss linear
Laplacian	<code>laplacianSchemes default</code>	Gauss linear corrected
Interpolation	<code>interpolationSchemes default</code>	linear
Surface normal gradient	<code>snGradSchemes default</code>	corrected
Wall distance	<code>wallDist method</code>	meshWave

The Euler scheme provides first-order temporal accuracy with unconditional stability for the selected time step sizes. The `linearUpwind` scheme for momentum convection combines upwind stability with reduced numerical diffusion compared to pure upwind differencing. The corrected surface normal gradient treatment accounts for mesh non-orthogonality, which is particularly important near the rotor surface and across AMI interfaces.

5 Results and Discussions

5.1 Performance Characteristics at Equilibrium TSR

The fluid-driven simulation with a calibrated damping coefficient ($c_{\text{damp}} = 6.28 \times 10^{-5} \text{ N}\cdot\text{m}\cdot\text{s}/\text{rad}$) naturally converges to an equilibrium tip speed ratio where aerodynamic torque balances the damping torque from the generator model. Unlike prescribed motion approaches that simulate arbitrary TSR values, this methodology produces a single equilibrium operating point reflecting realistic turbine dynamics under the specified loading condition.

Table 4 presents the performance metrics at equilibrium TSR, including power coefficient (C_p), torque coefficient (C_q), and thrust coefficient (C_T).

Table 4: Savonius rotor performance at equilibrium operating point (fluid-driven motion)

Equilibrium TSR	C_p	C_q	C_T
0.585	0.1816	0.3056	1.3670

The equilibrium TSR of 0.585 represents the self-consistent operating point where the rotor angular velocity ω satisfies the torque balance condition (Equation 14). At this speed, the aerodynamic torque generated by the flow interaction precisely equals the resistive torque from the damper, allowing steady state rotation. The corresponding power coefficient of 0.1816 indicates the fraction of kinetic energy extracted from the wind at this equilibrium condition. The torque coefficient of 0.3056 characterizes the rotor's ability to generate rotational moment, while the thrust coefficient of 1.3670 quantifies the structural loading in the streamwise direction, relevant for bearing and support structure design.

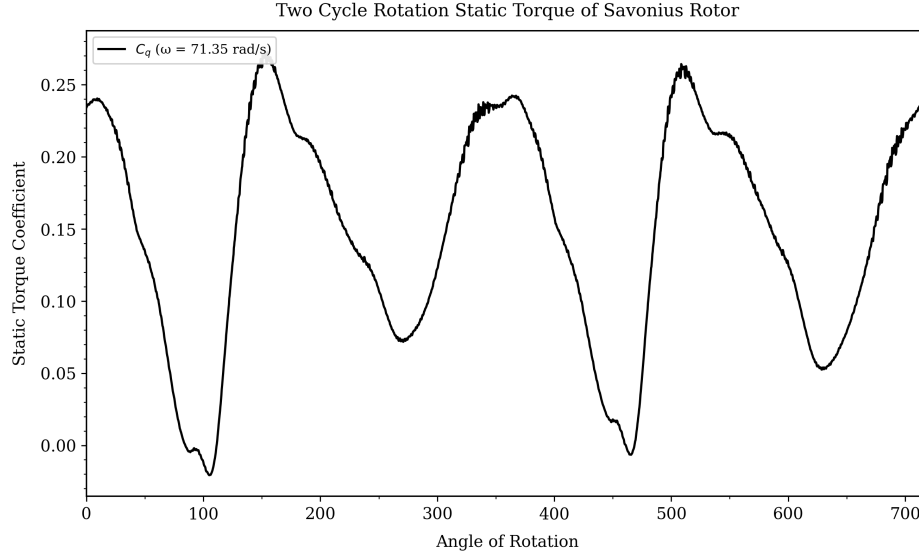


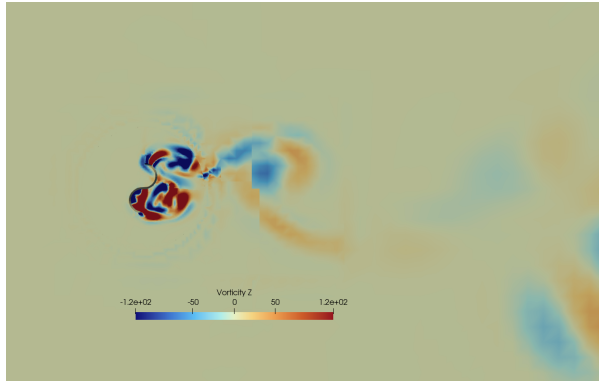
Figure 7: Instantaneous torque variation through two rotation cycle at Equilibrium TSR

Figure 7 illustrates the instantaneous torque variation as the rotor completes two full revolution. The Savonius rotor exhibits the characteristic double-peak pattern per 360° rotation, corresponding to the two blade configuration. Peak positive torque occurs at azimuthal angles of approximately 0° and 180° , when the concave blade faces the incoming flow. Minimum torque (potentially negative) occurs near 110° and 280° , where the convex blade surface dominates the flow interaction.

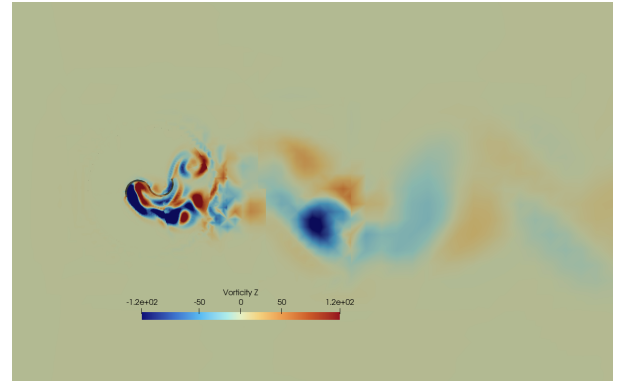
5.2 Flow Field Analysis

5.2.1 Vorticity Contours

Figure 9 presents vorticity magnitude contours at four different time instances throughout one rotation cycle, illustrating the evolution of wake structures.



(a) Vorticity contour at $\theta = 0^\circ$



(b) Vorticity contour at $\theta = 100^\circ$

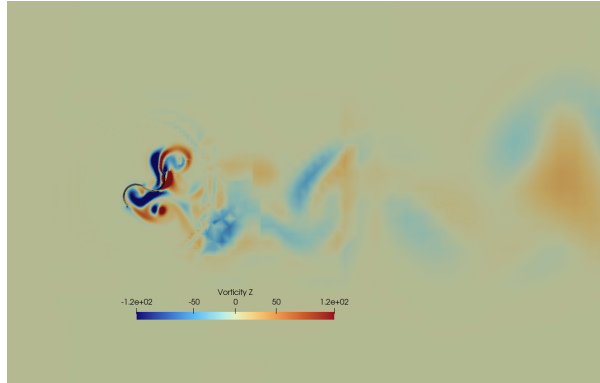
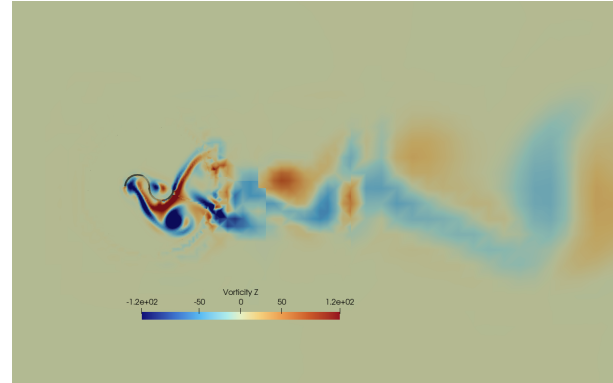
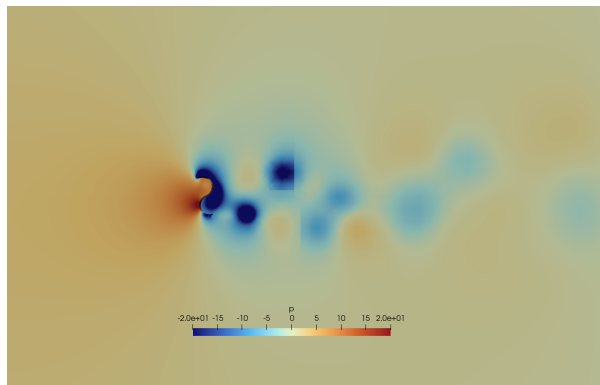
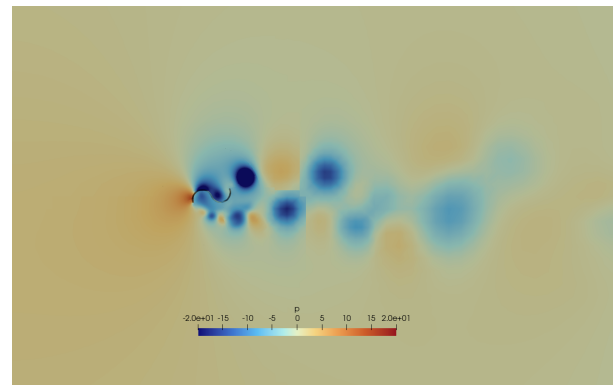
(c) Vorticity contour at $\theta = 225^\circ$ (d) Vorticity contour at $\theta = 330^\circ$

Figure 9: Vorticity contours through one complete rotation

The vorticity fields reveal the complex wake dynamics of the Savonius rotor across one complete rotation cycle. At $\theta = 0^\circ$, strong counter-rotating vortex pairs are shed from the blade tips as the advancing blade intercepts the incoming flow, while the returning blade experiences significant flow separation along its concave surface. By $\theta = 100^\circ$ and $\theta = 225^\circ$, the wake structures convect downstream and broaden laterally, with alternating positive and negative vorticity cores indicating a periodic vortex shedding pattern reminiscent of a bluff-body wake.

5.2.2 Pressure Distribution

(a) Pressure contour at $\theta = 0^\circ$ (b) Pressure contour at $\theta = 100^\circ$

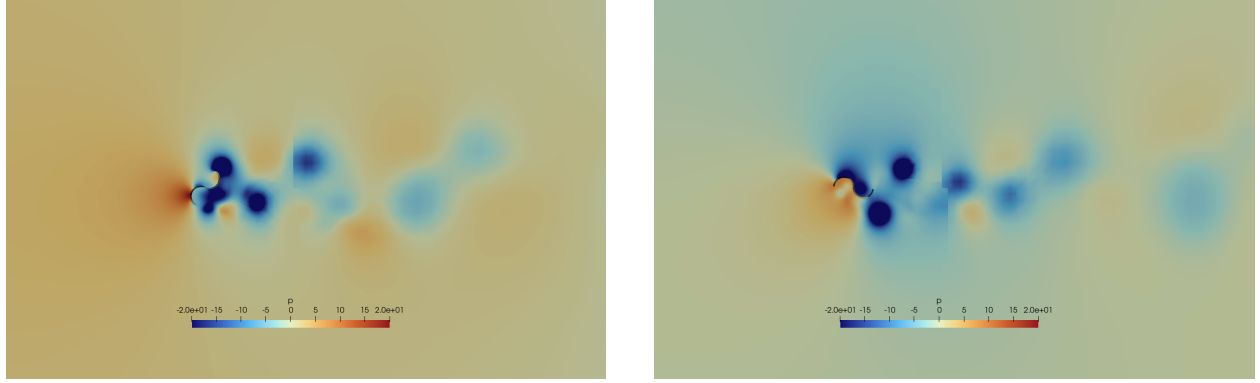
(c) Pressure contour at $\theta = 225^\circ$ (a) Pressure contour at $\theta = 330^\circ$

Figure 11: (d) Pressure contours through one complete rotation

The pressure distributions across one rotation cycle reveal the aerodynamic loading mechanism driving the rotor. At $\theta = 0^\circ$, a pronounced high-pressure region develops on the concave face of the advancing blade while a corresponding low-pressure zone forms on its convex rear surface, establishing the pressure differential responsible for net torque generation. As the rotor progresses through $\theta = 100^\circ$ and $\theta = 225^\circ$, this pressure asymmetry persists but migrates azimuthally with the blade position and the returning blade exhibits an unfavourable inverse pressure gradient that partially opposes the driving torque.

5.3 Startup Characteristics

A key advantage of the fluid-driven 6DoF simulation framework is the ability to predict realistic transient startup behavior from rest, capturing the rotor's natural acceleration under aerodynamic torque until reaching equilibrium. This capability is fundamentally unavailable in prescribed motion approaches, which require predetermined TSR specification and cannot simulate self-starting dynamics.

Figure 12 presents the startup transient behavior showing both angular velocity evolution and tip speed ratio development from initialization to equilibrium.

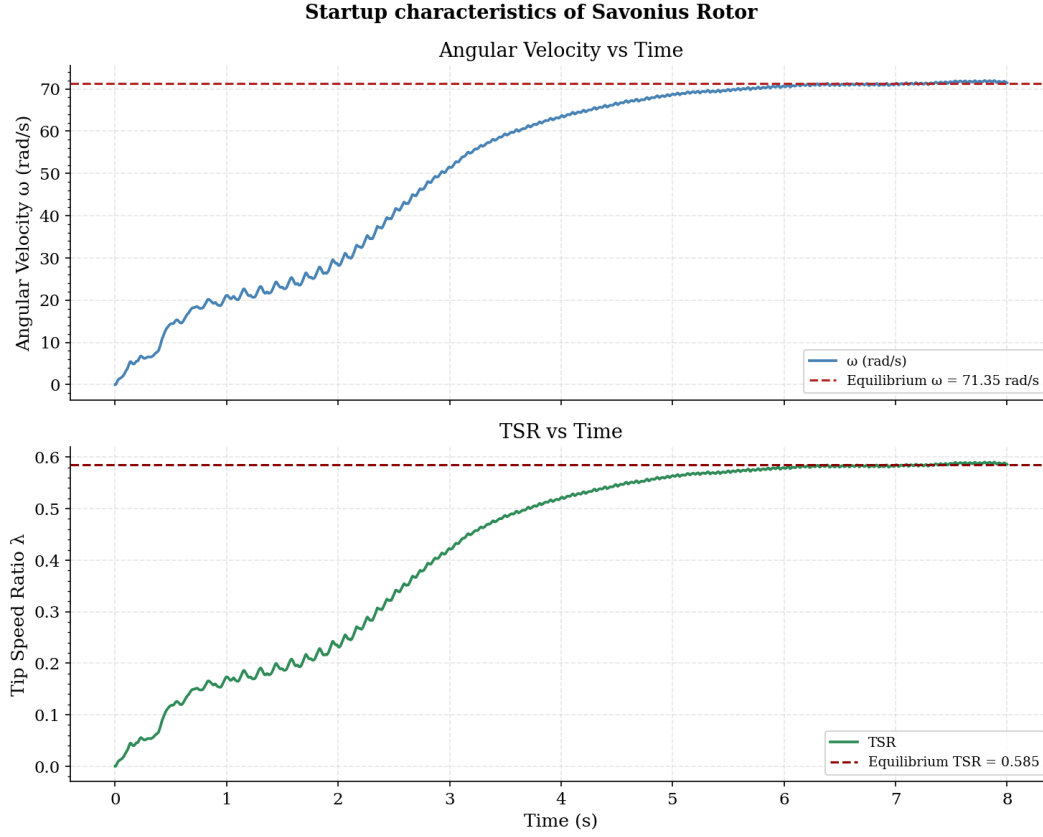


Figure 12: Savonius rotor's angular velocity and TSR evolution from rest to equilibrium

The rotor rapidly accelerates under positive aerodynamic torque, exhibiting a nonlinear acceleration characteristic of fluid-structure interaction. The angular velocity (Figure 12, top panel) demonstrates three distinct phases: (1) rapid initial acceleration from ~ 0.5 to 20 rad/s over approximately 1 second as the rotor overcomes inertia and blade-wake interactions establish, (2) progressive deceleration of acceleration as damping torque increases with rising angular velocity, and (3) asymptotic convergence to equilibrium angular velocity $\omega_{eq} = 71.35$ rad/s after approximately 6 seconds of simulation time.

The corresponding tip speed ratio evolves from nearly zero to the equilibrium value $TSR_{eq} = 0.585$, showing smooth monotonic increase with decreasing acceleration rate. The asymptotic approach to equilibrium confirms the torque balance condition (Equation 14) as ω approaches the equilibrium value, the rising damping torque ($\tau_{damp} = c_{damp} \cdot \omega$) progressively reduces net accelerating torque until equilibrium is achieved.

5.4 Comparison: Prescribed Motion vs. Fluid-Driven Approach

To validate the fluid-driven 6DoF methodology against traditional prescribed motion approaches, performance predictions from the present work are compared with the prescribed motion results from the savonius rotor study by Aryal et al. [8]. The comparison provides insight into methodological differences between prescribed motion and fluid-driven simulations on equivalent Savonius configurations.

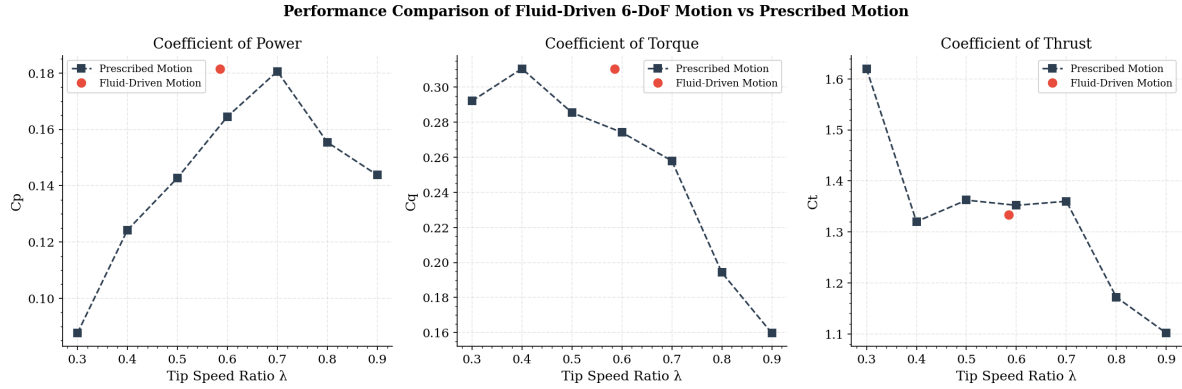


Figure 13: Performance comparison between prescribed motion (from [8]) and fluid-driven 6DoF approach showing power, torque, and thrust coefficients across TSR range (PLACEHOLDER)

Figure 13 presents side-by-side comparison of the power coefficient (C_p), torque coefficient (C_q), and thrust coefficient (C_T) predictions. The prescribed motion approach demonstrates a continuous performance envelope across the entire TSR range (0.3-0.9), with peak power coefficient of approximately 0.18 occurring at $\text{TSR} \approx 0.7$. This curve is generated by imposing angular velocities across a range of TSR values, with each point representing an independent simulation at a prescribed rotational speed.

In contrast, the fluid-driven 6DoF approach produces a single equilibrium operating point at $\text{TSR} = 0.585$ with $C_p = 0.18$, $C_q = 0.31$, and $C_T = 1.35$. Remarkably, this equilibrium point aligns closely with the prescribed motion performance curve in the moderate TSR region, validating that the self-consistent torque balance achieved by the 6DoF solver reproduces physically realistic performance comparable to externally imposed velocities. The fluid-driven result lies between the $\text{TSR} = 0.5$ and $\text{TSR} = 0.6$ points on the prescribed motion curve, consistent with equilibrium occurring where aerodynamic torque balances the generator loading torque.

5.5 Discussion

The fluid-driven simulation framework demonstrates that a Savonius VAWT rotor can achieve a physically self-consistent operating state through the coupling of the `sixDoFRigidBodyMotion` solver with transient AMI sliding mesh techniques. The equilibrium tip speed ratio of 0.585, emerging naturally from the torque balance between aerodynamic loading and the spherical angular damper, falls within the moderate-performance region of the Savonius operating envelope and compares favourably with the prescribed motion results of Aryal et al. [8], where peak $C_p \approx 0.18$ occurs near $\text{TSR} = 0.7$. The close agreement between the fluid-driven equilibrium point ($C_p = 0.1816$, $C_q = 0.3056$, $C_T = 1.367$) and the corresponding prescribed motion curve validates the physical consistency of the present methodology and confirms that the damper coefficient $c_{\text{damp}} = 6.28 \times 10^{-5} \text{ N}\cdot\text{m}\cdot\text{s}/\text{rad}$ is an effective surrogate for realistic generator loading at this operating condition.

The three-phase startup characteristics i.e. rapid inertial acceleration, progressive deceleration as damping torque grows, and asymptotic convergence to $\omega_{\text{eq}} = 71.35 \text{ rad/s}$ within approximately 6 seconds is entirely consistent with the drag-driven mechanism of the Savonius rotor. The characteristic double-peak torque signature observed in Figure 7 with positive maxima near $\theta = 0^\circ$ and 180° and near-zero minima near $\theta = 110^\circ$ and 280° reflects the known azimuthal torque ripple of the two-blade configuration. The vorticity and pressure contours further confirm that blade-wake interaction is the dominant flow mechanism. The alternating vortex shedding visible at $\theta = 100^\circ$ and $\theta = 225^\circ$ corresponds directly to the torque minima, as the convex returning blade operates in the disturbed wake of the advancing blade, generating an adverse pressure gradient that reduces net rotational moment.

By varying c_{damp} systematically, different generator load curves can be simulated to identify the damping coefficient that maximises C_p , without constructing a full TSR sweep through multiple prescribed-speed simulations. The present single-point result already indicates that the rotor operates in the ascending portion of the C_p vs TSR curve, suggesting that a marginally lower damping coefficient could shift the equilibrium toward the peak performance region near $\text{TSR} \approx 0.7$.

Limitations of the present study should be acknowledged. The laminar flow assumption ($Re \approx 28,000$) is defensible given the moderately low Reynolds number, but turbulent mixing effects in the rotor wake may be underestimated. The absence of rotor endplates in the CAD geometry means that three-dimensional tip-leakage flows are present and uncontrolled, which may slightly elevate the predicted thrust coefficient relative to a real shrouded installation. Finally, the mesh independence study is bounded by computational constraints at 528,884 cells.

6 Future Work

While this study successfully demonstrates a fluid-driven 6DoF framework for Savonius VAWT simulation, several extensions are identified that would broaden the applicability and fidelity of the methodology.

6.1 Parametric Study of Damping Coefficients

The present work employed a single calibrated damping coefficient ($c_{\text{damp}} = 6.28 \times 10^{-5} \text{ N}\cdot\text{m}\cdot\text{s}/\text{rad}$) targeting equilibrium at $\text{TSR} = 0.585$. A systematic parametric sweep of c_{damp} over the range $1 \times 10^{-5} - 2 \times 10^{-4} \text{ N}\cdot\text{m}\cdot\text{s}/\text{rad}$ would map the full operating envelope of the rotor from $\text{TSR} \approx 0.2$ to 1.2 within a single fluid-driven computational framework, replacing the multiple independent prescribed-speed simulations currently required to construct performance curves. This approach would also quantify the sensitivity of startup time and transient acceleration profile to generator loading, providing direct input for generator matching in small-scale wind energy applications.

6.2 Turbulence Modeling

The laminar flow assumption is justified at $Re \approx 28,000$ but may underestimate turbulent mixing in the rotor wake at higher inflow velocities. Incorporating a $k-\omega$ SST Reynolds-Averaged Navier-Stokes (RANS) closure, which is well-established for rotating machinery with adverse pressure gradients, would extend the validated operating range. Large Eddy Simulation (LES) could further resolve the unsteady vortex shedding structures observed in the present vorticity contours, providing higher-fidelity wake data for downstream turbine placement studies.

6.3 Geometric Variations

The 6DoF-AMI framework developed here is directly transferable to modified rotor geometries. Of particular interest are overlap ratio variations in the range 0–30%, twisted and helical blade profiles that distribute torque more uniformly across the rotation cycle, and endplate configurations that suppress three-dimensional tip-leakage flows. Multi-stage rotor designs, which offset blade pairs axially to reduce torque ripple, could also be evaluated with minimal changes to the simulation setup. Bio-inspired blade shapes, as investigated for VAWTs by Venkataraman and De [7], represent a further candidate for assessment within this self-consistent fluid-driven framework.

6.4 Experimental Validation

Wind tunnel measurements would provide the most direct validation of the present predictions. Particle Image Velocimetry (PIV) of the near-wake flow field could be compared against the vorticity contours presented in Section 5.2, while torque transducer recordings during motor-free startup from rest would validate the three-phase acceleration profile identified in Section 5.3. Such experimental data would also clarify the extent to which the laminar flow assumption affects torque ripple amplitude at the present Reynolds number.

6.5 Multi-Turbine Array Configurations

For urban distributed energy applications, rotor-rotor interaction effects are critical. Future work could extend the present single-rotor framework to two or three-turbine arrays, investigating optimal streamwise and lateral spacing to balance wake recovery and efficiency. Counter-rotating rotor pairs are of particular interest, as the torque ripple of adjacent turbines may partially cancel, reducing structural fatigue loading on shared support structures.

Acknowledgements

The author extends his deepest gratitude to his supervisors, Prof. Manabendra M. De (Academy of Scientific and Innovative Research, New Delhi) and Prof. Chandan Bose (University of Birmingham, UK), for their relentless support and valuable critiques throughout this study. Their attention to detail and academic rigour made the experience of learning and working on this project both insightful and exemplary.

The author's FOSSEE mentor, Mr. Pranay Pandey (IIT Bombay), provided the necessary guidance that helped navigate the technical hurdles encountered during the progression of this project. Sincere thanks are also extended to Mr. Manjil Sitoula for his assistance at a critical stage of the work.

Acknowledgement is made to the FOSSEE (Free and Open Source Software for Education) project at the Indian Institute of Technology Bombay for providing mentorship support and the platform through which this OpenFOAM Case Study Project was conducted.

The author also thanks the faculty and staff of the Department of Aerospace Engineering at IOE Pulchowk Campus, Tribhuvan University, whose resources and encouragement have been invaluable.

References

- [1] K Golecha, MA Kamoji, SB Kedare, and SV Prabhu. Review on savonius rotor for harnessing wind energy. *Wind Engineering*, 36(6):605–645, 2012.
- [2] MA Kamoji, SB Kedare, and SV Prabhu. Experimental investigations on the effect of overlap ratio and blade edge conditions on the performance of conventional savonius rotor. *Wind Engineering*, 32(2):163–178, 2008.
- [3] Nur Alom and Ujjwal K. Saha. Influence of blade profiles on savonius rotor performance: Numerical simulation and experimental validation. *Energy Conversion and Management*, 186: 267–277, 2019.
- [4] A. Damak, Z. Driss, and M.S. Abid. Experimental investigation of helical savonius rotor with a twist of 180° . *Renewable Energy*, 52:136–142, 2013.
- [5] Mohammed H. Ali. Experimental comparison study for savonius wind turbine of two & three blades at low wind speed. *International Journal of Modern Engineering Research (IJMER)*, 3 (5):2978–2986, 2013.
- [6] Ahmed S. Saad, Ibrahim I. El-Sharkawy, Shinichi Ookawara, and Mahmoud Ahmed. Performance enhancement of twisted-bladed savonius vertical axis wind turbines. *Energy Conversion and Management*, 209, 2020.
- [7] Priya Venkataraman and M De Manabendra. Numerical investigation of stand-still characteristics of a bio-inspired vertical axis wind turbine rotor. In *IOP Conference Series: Materials Science and Engineering*, volume 377. IOP Publishing, 2018.
- [8] Manu Aryal, Manabendra M De, and Chandan Bose. 3d numerical investigation of bio-inspired vertical axis wind turbine rotor using arbitrary mesh interface (ami). *FOSSEE OpenFOAM Case Study Project Report*, 2025.